

# Detecting quantum critical points at finite temperature via quantum teleportation: further models

G. A. P. Ribeiro and Gustavo Rigolin\*

*Departamento de Física, Universidade Federal de São Carlos, 13565-905, São Carlos, SP, Brazil*

(Dated: January 17, 2024)

In [Phys. Rev. A **107**, 052420 (2023)] we showed that the quantum teleportation protocol can be used to detect quantum critical points (QCPs) associated with a couple of different classes of quantum phase transitions, even when the system is away from the absolute zero temperature ( $T = 0$ ). Here, working in the thermodynamic limit (infinite chains), we extend the previous analysis for several other spin-1/2 models. We investigate the usefulness of the quantum teleportation protocol to detect the QCPs of those models when the temperature is either zero or greater than zero. The spin chains we investigate here are described by the XXZ model, the XY model, and the Ising model, all of them subjected to an external magnetic field. Specifically, we use a pair of nearest neighbor qubits from an infinite spin chain at thermal equilibrium with a reservoir at temperature  $T$  as the resource to execute the quantum teleportation protocol. We show that the ability of this pair of qubits to faithfully teleport an external qubit from the chain is dramatically affected as we cross the QCPs related to the aforementioned models. The results here presented together with the ones of [Phys. Rev. A **107**, 052420 (2023)] suggest that the quantum teleportation protocol is a robust and quite universal tool to detect QCPs even when the system of interest is far from the absolute zero temperature.

## I. INTRODUCTION

A quantum phase transition (QPT) is a qualitative change in the ground state of a many-body system that theoretically happens at the absolute zero ( $T = 0$ ) as we slowly change the system's Hamiltonian  $H$  [1–4]. This qualitative change in the physical properties of the system is driven by genuine quantum fluctuations (Heisenberg uncertainty principle) since at  $T = 0$  there are no thermal fluctuations at stake. A QPT is usually characterized by a symmetry change in the system's ground state and by the emergence of an order parameter such as the total magnetization that is no longer zero after a ferromagnetic QPT.

Most of the theoretical analysis studying QPTs, in particular those employing quantum information theory concepts, assume that the system is at  $T = 0$  [5–8]. Experimentally, though, we cannot cool a many-body system to  $T = 0$  (third law of thermodynamics) and thus it is crucial to build and develop robust tools to characterize QPTs assuming the system is at finite  $T$ . This becomes even more important whenever  $kT \approx \Delta E$ , where  $k$  is Boltzmann constant and  $\Delta E$  is the energy gap between the system's ground and first excited states. In this scenario thermal fluctuations cannot be ignored and it is a necessity to develop robust quantum critical point (QCP) detectors that still work in this regime. For instance, the entanglement of formation (EoF) [9] and the magnetic susceptibility no longer detect a QPT in spin chains when  $T > 0$  and other tools are needed to detect a QCP at finite  $T$  [10, 11].

A very useful and robust tool to detect QCPs at fi-

nite  $T$  is quantum discord (QD), usually called thermal quantum discord (TQD) in this context [11]. Although very successful in detecting QCPs when  $T > 0$  [11], QD [12, 13] has its handicaps. The computation of QD is NP-complete [14], which implies that the evaluation of QD is an intractable problem for systems described by a large Hilbert space [15]. Also, QD has no operational interpretation. We do not have an experimental procedure to directly measure QD. We can only compute QD if we have access to the system's whole density matrix.

We should note that, recently, a quantity derived from the quantum coherence [16–18] was shown to be very robust to detect QCPs using finite  $T$  data, outperforming QD for certain models [19]. This quantity was called the logarithm of the spectrum of the quantum coherence ( $L_{QC}$ ) [19]. But similarly to QD,  $L_{QC}$  has no operational interpretation, i.e., there is no experimental procedure for its direct determination. One needs the density matrix (measured or calculated) of the system investigated to compute it. For a two-qubit density matrix  $\rho$ , this means that we always need to know (compute or measure) its one- and two-point correlation functions. Furthermore, to compute  $L_{QC}$  one needs the eigenvalues of the following squared commutator,  $[\rho, K]^2$ , whose computational complexity does not scale linearly with the size of the system as we increase its Hilbert space dimension. The computation of  $L_{QC}$  has also an arbitrariness in the choice of the observable “K” [19]. Depending on the observable chosen,  $L_{QC}$  does not detect QCPs. And for high dimensional systems, the number of observables becomes very large, making it difficult to test all cases and increasing the arbitrariness for the choice of the right observable.

In Ref. [20] we developed a QCP detection tool that has the most useful characteristics of TQD in spotlighting QCPs at finite  $T$  and, in addition, is free from the

---

\*Electronic address: rigolin@ufscar.br

handicaps outlined above. That tool is built on the quantum teleportation protocol [21–24] and will be described in Sec. II. We should also mention another recent tool to detect QCPs at  $T = 0$  based on the quantum energy teleportation protocol [25, 26]. It was show in Refs. [27–30] that for several models the amount of teleported energy depends on the phase of the system.

In this work we apply the teleportation based QCP detector of Ref. [20] to several other models. Here we study the XXZ model subjected to an external magnetic field, complementing the analysis of Ref. [20], where we studied this model without an external field. We also investigate the efficiency of the teleportation based QCP detector in spotlighting the QCPs of the Ising model and of the XY model in a transverse magnetic field. As we will see, the present tool allows us to determine all the QCPs of these models even if the system’s temperature is not zero.

## II. THE TELEPORTATION BASED CRITICAL POINT DETECTOR

Let us start by reviewing the standard teleportation protocol [21], in particular its mathematical description when the shared entangled state between Alice and Bob is not a pure state [23, 24]. We label the qubits from the entangled resource shared by Alice and Bob as qubits 2 and 3, respectively (see Fig. 1). The density matrix describing those qubits is  $\rho_{23}$ . The qubit that Alice wants to teleport to Bob is a pure state external to the spin chain and its density matrix is  $\rho_1 = |\psi\rangle\langle\psi|$  (qubit 1 in Fig. 1), where

$$|\psi\rangle = r|0\rangle + \sqrt{1-r^2}e^{i\chi}|1\rangle = \cos(\theta/2)|0\rangle + \sin(\theta/2)e^{i\chi}|1\rangle, \quad (1)$$

with  $0 \leq r \leq 1$  ( $0 \leq \theta \leq \pi$ ) and  $0 \leq \chi < 2\pi$ .

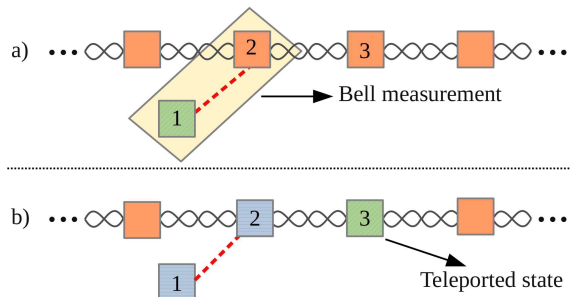


FIG. 1: (color online) a) Alice and Bob agree that spins 2 and 3 of the spin chain are the entangled resource used to teleport the external qubit 1. Alice implements a Bell measurement (BM) onto qubits 1 and 2. b) Alice tells Bob her BM result via a classical communication channel. Bob then applies a unitary operation on qubit 3, depending on the news received from Alice. This finishes one run of the protocol.

At the beginning of the teleportation protocol, the

state describing the three qubits is

$$\rho = \rho_1 \otimes \rho_{23}. \quad (2)$$

At the end of the protocol (after one run of the protocol), Bob’s spin (qubit 3) is given by [20, 23]

$$\rho_{B_j} = \frac{U_j Tr_{12}[P_j \rho P_j] U_j^\dagger}{Q_j(|\psi\rangle)}. \quad (3)$$

Here  $Tr_{12}$  is the partial trace on Alice’s spins (qubits 1 and 2),  $j$  denotes the Bell measurement (BM) result obtained by Alice ( $j = \Psi^-, \Psi^+, \Phi^-, \Phi^+$ ), and  $P_j$  represents the four projectors describing the BMs,

$$P_{\Psi^\pm} = |\Psi^\pm\rangle\langle\Psi^\pm|, \quad (4)$$

$$P_{\Phi^\pm} = |\Phi^\pm\rangle\langle\Phi^\pm|, \quad (5)$$

with the Bell states given by

$$|\Psi^\mp\rangle = (|01\rangle \mp |10\rangle)/\sqrt{2}, \quad (6)$$

$$|\Phi^\mp\rangle = (|00\rangle \mp |11\rangle)/\sqrt{2}. \quad (7)$$

The probability to measure a given Bell state  $j$  is [20, 23]

$$Q_j(|\psi\rangle) = Tr[P_j \rho] \quad (8)$$

and the unitary correction that Bob should implement on his qubit after receiving the news about Alice’s BM result is  $U_j$ .

The unitary operation that Bob should apply on his qubit at the end of a given run of the protocol also depends on the entangled state shared with Alice. When they share a maximally entangled pure state  $|k\rangle$  (Bell state) [21], the set  $S_k$  below lists the four unitary operations that Bob should apply on his qubit [20, 23],

$$S_{\Phi^+} = \{U_{\Phi^+}, U_{\Phi^-}, U_{\Psi^+}, U_{\Psi^-}\} = \{\mathbb{1}, \sigma^z, \sigma^x, \sigma^z \sigma^x\}, \quad (9)$$

$$S_{\Phi^-} = \{U_{\Phi^+}, U_{\Phi^-}, U_{\Psi^+}, U_{\Psi^-}\} = \{\sigma^z, \mathbb{1}, \sigma^z \sigma^x, \sigma^x\}, \quad (10)$$

$$S_{\Psi^+} = \{U_{\Phi^+}, U_{\Phi^-}, U_{\Psi^+}, U_{\Psi^-}\} = \{\sigma^x, \sigma^z \sigma^x, \mathbb{1}, \sigma^z\}, \quad (11)$$

$$S_{\Psi^-} = \{U_{\Phi^+}, U_{\Phi^-}, U_{\Psi^+}, U_{\Psi^-}\} = \{\sigma^z \sigma^x, \sigma^x, \sigma^z, \mathbb{1}\}, \quad (12)$$

where  $\mathbb{1}$  is the identity matrix and  $\sigma^\alpha$ ,  $\alpha = x, y, z$ , is the standard Pauli matrix [31]. In other words,  $S_k$  represents the set of unitary operations that Bob should apply if Alice and Bob share the Bell state  $|k\rangle$ , with  $k = \Psi^\pm, \Phi^\pm$ . For instance,  $S_{\Phi^+}$  means that they share the state  $|\Phi^+\rangle$  and that if Alice’s BM result is  $|\Phi^+\rangle$ ,  $|\Phi^-\rangle$ ,  $|\Psi^+\rangle$ , or  $|\Psi^-\rangle$ , the corresponding unitary corrections that Bob should apply is  $\mathbb{1}, \sigma^z, \sigma^x$ , or  $\sigma^z \sigma^x$ .

In the models we will be studying in what follows, the state  $\rho_{23}$  shared between Alice and Bob is a mixed state. In one quantum phase  $\rho_{23}$  is closer to one of the four Bell states and in another phase closer to a different one. Thus, when studying the QCPs of a spin chain we will employ the four sets of unitary operations above, eventually picking the set yielding the optimal teleportation protocol.

To determine the optimal teleportation protocol, we need a quantitative measure of the similarity between the teleported state at the end of a run of the protocol and the initial state teleported by Alice. As usual, we employ the fidelity [32] to quantify the similarity between those states. When we have a pure input state the fidelity is

$$F_j(|\psi\rangle, S_k) = \langle \psi | \rho_{B_j} | \psi \rangle, \quad (13)$$

where  $|\psi\rangle$  is given by Eq. (1) and  $\rho_{B_j}$  by Eq. (3). Note that the subscript  $j$  denotes which Bell state Alice obtained after implementing the BM on qubits 1 and 2. For a teleported state exactly equal to the input state we have  $F_j = 1$ , while  $F_j = 0$  if the teleported state is orthogonal to the input. We should note that in addition to depending on the initial state,  $F_j$  also depends through  $\rho_{B_j}$  on the entangled state shared by Alice and Bob and on the set of unitary operations  $S_k$  that he can apply on his qubit. In this work, the entangled resource is determined by the model being investigated and we can freely choose  $|\psi\rangle$  and  $S_k$ , with  $k = \Psi^\mp, \Phi^\mp$ .

If we fix the input state, after a single run of the protocol its fidelity is given by Eq. (13) and after several runs of the protocol the mean fidelity (efficiency) is [20, 23, 24, 33]

$$\overline{F}(|\psi\rangle, S_k) = \sum_{j=\Psi^\mp, \Phi^\mp} Q_j(|\psi\rangle) F_j(|\psi\rangle, S_k). \quad (14)$$

Equation (14), as we show here, is the building block leading to the most sharp QCP detector and can be understood as the efficiency of the teleportation protocol for a fixed input state and a given set  $S_k$  of unitary operations.

In order to obtain an input state independent measure of the efficiency of the quantum teleportation protocol, we take the average over all states on the Bloch sphere. This Bloch sphere average is equivalent to assuming in Eq. (1) that  $r^2$  and  $\gamma$  are two independent continuous random variables over their domain [24, 33]. We can write this state independent mean fidelity as [23, 24, 33]

$$\langle \overline{F}(S_k) \rangle = \int_{\Omega} \overline{F}(|\psi\rangle, S_k) \mathcal{P}(|\psi\rangle) d|\psi\rangle. \quad (15)$$

In Eq. (15) the integration over the sample space  $\Omega$  includes all qubits on the Bloch sphere and  $\mathcal{P}(|\psi\rangle)$  is the appropriate uniform probability distribution over  $\Omega$  [20]. From now on, the quantity defined in Eq. (14) will be called ‘‘mean fidelity’’ and the quantity given by Eq. (15) will be denoted ‘‘average fidelity’’.

### III. THE XXZ MODEL IN AN EXTERNAL FIELD

The Hamiltonian describing the XXZ model in an external longitudinal field is ( $\hbar = 1$ )

$$H = \sum_{j=1}^L \left( \sigma_j^x \sigma_{j+1}^x + \sigma_j^y \sigma_{j+1}^y + \Delta \sigma_j^z \sigma_{j+1}^z - \frac{h}{2} \sigma_j^z \right). \quad (16)$$

We will be dealing with a spin-1/2 chain in the thermodynamic limit ( $L \rightarrow \infty$ ) satisfying periodic boundary conditions ( $\sigma_{L+1}^\alpha = \sigma_1^\alpha$ ). The subscript  $j$  above means that  $\sigma_j^\alpha$  acts on the spin at the lattice site  $j$ . The anisotropy  $\Delta$  is our tuning parameter and  $h$  is the external magnetic field, which will be fixed as we vary  $\Delta$  across the QCPs for this model.

At  $T = 0$  and for a finite external magnetic field  $h$ , this model has two QCPs [34–40]. At  $\Delta_1$  we have the first QCP, where the ground state changes from a ferromagnetic ( $\Delta < \Delta_1$ ) to a critical antiferromagnetic phase ( $\Delta_1 < \Delta < \Delta_2$ ). At  $\Delta_2$  another phase transition takes place, with the system becoming an Ising-like antiferromagnet for  $\Delta > \Delta_2$ . The two QCPs depend on  $h$  and are given as follows [34–40].

The critical point  $\Delta_1$  is obtained by solving the following equation once we fix the value of  $h$ ,

$$h = 4J(1 + \Delta_1). \quad (17)$$

The critical point  $\Delta_2$  is the solution of

$$h = 4 \sinh(\eta) \sum_{j=-\infty}^{\infty} \frac{(-1)^j}{\cosh(j\eta)}, \quad (18)$$

where  $\eta = \cosh^{-1}(\Delta_2)$ . In Table I we list the QCPs for the two values of  $h$  that we will be dealing here and also the QCPs for the zero field case ( $h = 0$ ).

TABLE I: Quantum critical points for different values of the external field  $h$ . The values for  $\Delta_2$  when  $h > 0$  are accurate within an error of  $\pm 0.001$ .

|            | $h = 0$ | $h = 6$ | $h = 12$ |
|------------|---------|---------|----------|
| $\Delta_1$ | -1.00   | 0.50    | 2.00     |
| $\Delta_2$ | 1.00    | 3.299   | 4.875    |

A physical system in equilibrium with a thermal reservoir at temperature  $T$  is described by the canonical ensemble density matrix. As such, the density matrix describing the thermalized spin chain (16) is  $\varrho = e^{-H/kT}/Z$ , where  $Z = \text{Tr}[e^{-H/kT}]$  is the partition function and  $k$  is Boltzmann’s constant. To obtain the density matrix describing a pair of nearest neighbor spins, we trace out from  $\varrho$  all the other spins. This leads to [11]

$$\rho_{23} = \begin{pmatrix} a & 0 & 0 & 0 \\ 0 & b & c & 0 \\ 0 & c & b & 0 \\ 0 & 0 & 0 & d \end{pmatrix}, \quad (19)$$

where

$$a = \frac{1 + 2 \langle \sigma_2^z \rangle + \langle \sigma_2^z \sigma_3^z \rangle}{4}, \quad (20)$$

$$b = \frac{1 - \langle \sigma_2^z \sigma_3^z \rangle}{4}, \quad (21)$$

$$c = \frac{\langle \sigma_2^x \sigma_3^x \rangle}{2}, \quad (22)$$

$$d = \frac{1 - 2 \langle \sigma_2^z \rangle + \langle \sigma_2^z \sigma_3^z \rangle}{4}. \quad (23)$$

Note that the translational symmetry of  $H$  implies that  $\langle \sigma_j^\alpha \rangle = \langle \sigma_k^\alpha \rangle$  and  $\langle \sigma_j^\alpha \sigma_{j+1}^\beta \rangle = \langle \sigma_k^\alpha \sigma_{k+1}^\beta \rangle$ , for any value of  $j, k$ .

In the thermodynamic limit, the calculation for arbitrary values of  $T$ ,  $\Delta$ , and  $h$  of the one-point correlation function  $\langle \sigma_j^z \rangle = Tr[\sigma_j^z \varrho]$  and of the two-point correlation functions  $\langle \sigma_j^\alpha \sigma_{j+1}^\alpha \rangle = Tr[\sigma_j^\alpha \sigma_{j+1}^\alpha \varrho]$ , where  $\alpha = x, z$ , was carried out in Refs. [36–39] and reviewed in Refs. [11]. In the Appendix A we show the behavior of  $\langle \sigma_j^z \rangle$  and  $\langle \sigma_j^\alpha \sigma_{j+1}^\alpha \rangle$  for several values of  $T$ ,  $\Delta$ , and  $h$ .

If we use Eqs. (1), (2), and (19), a direct calculation with Eq. (8) gives

$$Q_{\Psi^\pm}(|\psi\rangle) = [1 - z \cos \theta]/4, \quad (24)$$

$$Q_{\Phi^\pm}(|\psi\rangle) = [1 + z \cos \theta]/4, \quad (25)$$

where

$$z = \langle \sigma_j^z \rangle = Tr[\sigma_j^z \varrho]. \quad (26)$$

Contrary to the case with no field [20], where  $Q_j(|\psi\rangle) = 1/4$  for all  $j$  and  $|\psi\rangle$ , the chances of Alice measuring a given Bell state depend on the input state  $|\psi\rangle$  through  $\theta$  and on the one-point correlation function  $z$ . However, averaging over the whole Bloch sphere [20], it is not difficult to see that  $\langle Q_j(|\psi\rangle) \rangle = 1/4$  for any  $j$ . Note that one should not confuse the Bloch sphere average notation  $\langle \rangle$  introduced in Eq. (15) with the standard notation for correlation functions as given, for instance, in Eq. (26).

With the aid of Eqs. (13), (24) and (25), we can compute the mean fidelity (14) for each one of the four sets of unitary operations available to Bob,

$$\overline{F}(|\psi\rangle, S_{\Psi^-}) = f(r, -xx, zz), \quad (27)$$

$$\overline{F}(|\psi\rangle, S_{\Psi^+}) = f(r, xx, zz), \quad (28)$$

$$\overline{F}(|\psi\rangle, S_{\Phi^-}) = g(r, \chi, -xx, zz), \quad (29)$$

$$\overline{F}(|\psi\rangle, S_{\Phi^+}) = g(r, \chi, xx, zz), \quad (30)$$

where

$$f(r, xx, zz) = [1 + 4r^2(1 - r^2)(xx + zz) - zz]/2, \quad (31)$$

$$g(r, \chi, xx, zz) = [1 + (1 - 2r^2)^2 zz + 4r^2(1 - r^2)xx \cos(2\chi)]/2, \quad (32)$$

$$xx = \langle \sigma_j^x \sigma_{j+1}^x \rangle = Tr[\sigma_j^x \sigma_{j+1}^x \varrho], \quad (33)$$

$$zz = \langle \sigma_j^z \sigma_{j+1}^z \rangle = Tr[\sigma_j^z \sigma_{j+1}^z \varrho]. \quad (34)$$

Looking at Eqs. (31) and (32), we realize that they do not depend on the one-point correlation function (26). They only depend on the two-point correlation functions (33) and (34). Hence, the four mean fidelities (27)-(30) depend only on the two-point correlation functions too. Moreover, this also implies that the expressions given by Eqs. (27)-(32) are formally the same as the ones we have for the XXZ model without an external field [20]. Thus, the calculations leading to the maximum mean fidelity and to the maximum averaged fidelity reported in Ref. [20] can be literally carried over to the present case.

Maximizing over all pure states and over  $S_k$  we get for the maximum mean fidelity [20],

$$\overline{\mathcal{F}} = \max_{\{|\psi\rangle, S_k\}} \overline{F}(|\psi\rangle, S_k) = \max \left[ \frac{1 + |zz|}{2}, \frac{1 + |xx|}{2} \right]. \quad (35)$$

The maximum or minimum of  $\overline{F}(|\psi\rangle, S_k)$  occur for the input states  $|\psi\rangle = |0\rangle, |1\rangle$ , and  $(|0\rangle + e^{ix}|1\rangle)/\sqrt{2}$ . The role of these states in maximizing or minimizing  $\overline{F}(|\psi\rangle, S_k)$  depends on the sign and on the magnitude of the two-point correlation functions  $xx$  and  $zz$ .

On the other hand, Eq. (15) implies that [20]

$$\langle \overline{F}(S_{\Psi^\pm}) \rangle = (3 \pm 2xx - zz)/6, \quad (36)$$

$$\langle \overline{F}(S_{\Phi^\pm}) \rangle = (3 + zz)/6. \quad (37)$$

Maximizing over all sets  $S_k$  we obtain the maximum average fidelity,

$$\langle \overline{\mathcal{F}} \rangle = \max_{\{S_k\}} \langle \overline{F}(S_k) \rangle = \max \left[ \frac{3 + 2|xx| - zz}{6}, \frac{3 + zz}{6} \right]. \quad (38)$$

Equations (35) and (38) are the two teleportation based QCP detectors that turned out to be extremely useful and robust to detect at finite  $T$  the QCPs for the XXZ model with no external field [20]. Our goal now is to investigate their ability in detecting the QCPs for this model when we turn on the external magnetic field.

In Figs. 2 and 3 we show  $\overline{\mathcal{F}}$  as a function of  $\Delta$  for several temperatures and for the two external fields given in Tab. I.

For  $T = 0$  it is clear from Figs. 2 and 3, in particular the insets, that both QCPs ( $\Delta_1$  and  $\Delta_2$ ) are detected by discontinuities in the derivatives of  $\overline{\mathcal{F}}$  with respect to  $\Delta$  as we cross the QCPs. We also see two other discontinuities in the derivatives of  $\overline{\mathcal{F}}$  for values of  $\Delta$  between the two QCPs, i.e., for  $\Delta_1 < \Delta < \Delta_2$ . One of these extra cusp-like behavior for  $\overline{\mathcal{F}}$  as a function of  $\Delta$  is also seen when we study the behavior of the thermal quantum discord as a function of  $\Delta$  [11]. Also, preliminary calculations [41] show that the logarithm of the spectrum of the quantum coherence ( $L_{QC}$ ) [19] also has a cusp not related to a quantum phase transition. These cusps are robust to temperature changes since they are not smoothed out as we increase the temperature (see Figs. 2 and 3).

The underlying reason for these two cusps of  $\overline{\mathcal{F}}$  is its particular functional form. As we change  $\Delta$ , the magnitudes of the two-point correlation functions  $xx$  and  $zz$  change. As we cross the two cusps, the correlation function with the greater magnitude changes. This change is reflected in a discontinuity in the value of  $\overline{\mathcal{F}}$  [see Eq. (35)].

As an illustrative example, in Fig. 4 we show for  $T = 0$  the behavior of  $|xx|$  and  $|zz|$  as a function of  $\Delta$  assuming  $h = 6.0$ . A similar behavior is seen for  $T > 0$  and also when we have  $h = 12.0$ . Looking at Fig. 4, it is clear that  $|xx| > |zz|$  in the yellow-shaded region, while  $|xx| < |zz|$  outside that region. The yellow-shaded region was drawn such that it represents the region between the two cusps of  $\overline{\mathcal{F}}$  that are not related to QPTs (see Fig. 2). Looking

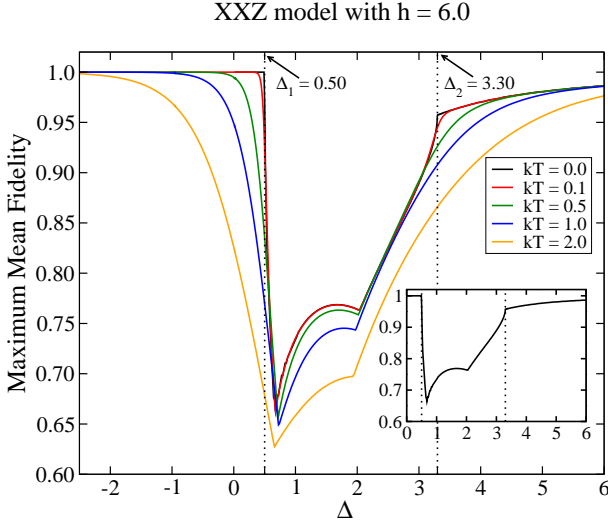


FIG. 2: (color online)  $\overline{\mathcal{F}}$ , Eq. (35), as a function of  $\Delta$  with  $h = 6.0$  [see Eq. (16)]. At  $T = 0$  (see inset), both QCPs are detected by a discontinuity in the derivatives of  $\overline{\mathcal{F}}$  with respect to  $\Delta$ . For  $T > 0$ , these discontinuities in the derivatives are smoothed out. The maxima (or minima) of the derivatives are displaced away from the critical points. However, for  $kT \lesssim 0.5$  these extremum values lie close together and by extrapolating to  $kT \rightarrow 0$  we are able to infer the correct critical points. The dotted lines mark the QCPs and for the solid curves the temperature increases from top to bottom. Here and in all other graphs all quantities are dimensionless.

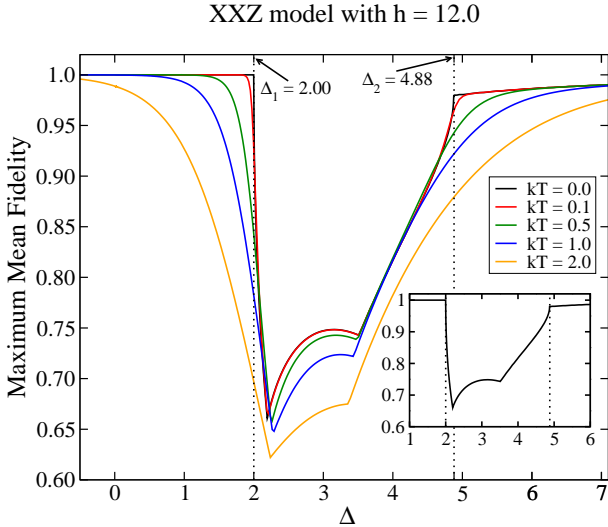


FIG. 3: (color online) Same as Fig. 2 but now  $h = 12.0$ . The dotted lines mark the QCPs and for the solid curves the temperature increases from top to bottom.

at Fig. 4, it is clear that the boundaries of the yellow-shaded region coincide with the two values of  $\Delta$  in which the roles of  $xx$  and  $zz$  are exchanged in the evaluation of (35) and (38). It is this property of  $|xx|$  and  $|zz|$  as we cross those two points that causes the two extra cusps seen in  $\overline{\mathcal{F}}$ .

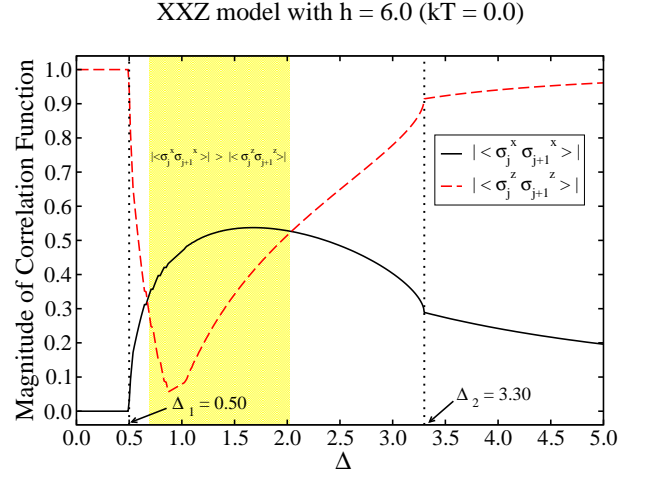


FIG. 4: (color online) Magnitudes of  $\langle \sigma_j^x \sigma_{j+1}^x \rangle$  and  $\langle \sigma_j^z \sigma_{j+1}^z \rangle$  as a function of  $\Delta$  when  $h = 6.0$  and  $T = 0$ . The yellow-shaded region is the region between the two cusps of  $\overline{\mathcal{F}}$  that do not correspond to QCPs.

It is worth mentioning that when we do not have an external field ( $h = 0$ ), the QCPs  $\Delta_1$  and  $\Delta_2$  are located exactly at the points in which  $|xx| = |zz|$ . This is why  $\overline{\mathcal{F}}$  is very robust in detecting those two QCPs for finite  $T$ , retaining its cusp-like behavior at the QCPs as we increase  $T$  [20]. When  $h = 0$  we only have two discontinuities, exactly at the locations of the two QCPs [20]. When  $h \neq 0$ , on the other hand, the points where  $|xx| = |zz|$  are shifted away from the QCPs and four cusps instead of two are seen when  $T = 0$ . Two of them are related to the two QCPs and the other two are associated with the points where  $|xx| = |zz|$ .

We can also better understand the behavior of  $\overline{\mathcal{F}}$  if we analyze the behavior of the following quantity,

$$\overline{F}(S_k) = \max_{\{|\psi\rangle\}} \overline{F}(|\psi\rangle, S_k). \quad (39)$$

Equation (39) is obtained from  $\overline{F}(|\psi\rangle, S_k)$  by maximizing it over all input states only. In this way, as we show in Fig. 5, we are able to study how  $\overline{F}(S_k)$  behaves for each one of the possible values of  $k$ ,

$$\overline{F}(S_{\Psi\pm}) = \max \left[ \frac{1 - zz}{2}, \frac{1 \pm xx}{2} \right], \quad (40)$$

$$\overline{F}(S_{\Phi\pm}) = \max \left[ \frac{1 + zz}{2}, \frac{1 + |xx|}{2} \right]. \quad (41)$$

Looking at Fig. 5, we notice that before  $\Delta_1$  (the first QCP) and up to where  $|xx| = |zz|$  (before the yellow-shaded region), the maximum mean fidelity  $\overline{\mathcal{F}}$  is given by  $\overline{F}(S_{\Phi\pm})$ . In the yellow-shaded region, we have either  $\overline{F}(S_{\Phi\pm})$  or  $\overline{F}(S_{\Psi-})$  as the maximum mean fidelity. After the yellow-shaded region,  $\overline{F}(S_{\Psi\pm})$  dominates. Furthermore, the points where the roles of  $\overline{F}(S_{\Psi\pm})$  and  $\overline{F}(S_{\Phi\pm})$  are exchanged in furnishing the greatest mean fidelity occur exactly where  $|xx| = |zz|$  (the boundaries of the

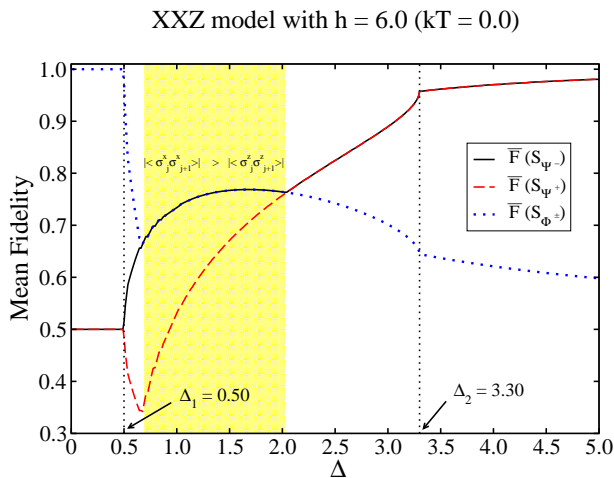


FIG. 5: (color online)  $\overline{F}(S_k)$ , Eq. (39), as a function of  $\Delta$  when  $T = 0$  and  $h = 6.0$ .

yellow-shaded region). This is why we see the two cusps of  $\overline{F}$  that are not related to QPTs. The other two derivative discontinuities, associated with the two QCPs, are due to the particular behavior of the two-point correlation functions at those points. The discontinuities in the derivatives of  $zz$  in the first and second QCPs are reflected in the discontinuities of the derivatives of  $\overline{F}$  at those points (cf. Figs. 4 and 5). Had we worked with the minimum mean fidelity [20], the relevant two-point correlation function would be  $xx$ .

When  $T > 0$ , the cusps located at the two QCPs are smoothed out and displaced away. The other two cusps are not smoothed out although being displaced too. As such, in order to determine the two QCPs in this scenario, we follow a similar strategy used in Ref. [11] to deal with the smoothing out of the cusps of the thermal quantum discord around the QCPs at finite  $T$ . As we increase the temperature, the discontinuities in the derivatives of  $\overline{F}$  that occur exactly at the QCPs when  $T = 0$  are now manifested in very high values for the magnitudes of those derivatives, with those maxima displaced from the correct locations of the QCPs. However, for  $kT \lesssim 0.5$  the maximum (or minimum) of the derivatives as a function of  $kT$  lie more or less along a straight line and by extrapolating to zero from a few finite  $T$  data we can correctly predict the exact locations of the two QCPs.

In the upper panel of Fig. 6, we show as a function of  $T$  the values of  $\Delta$  where we find the maximum of  $|dy/d\Delta|$ , with  $y$  representing the quantities shown in Fig. 6. In the upper panel we picked the maxima of  $|dy/d\Delta|$  around  $\Delta_1$ . In the lower panel of Fig. 6, we show as a function of  $T$  the spots of the maximum values of  $|d^2y/d\Delta^2|$  about  $\Delta_2$ . Note that although in Fig. 6 we chose the external field to be  $h = 12.0$ , the analysis reported below applies to other values of fields as well.

For  $kT = 0, 0.1, 0.2, 0.3, 0.4$ , and  $0.5$ , we computed  $\overline{F}$ ,  $\langle \overline{F} \rangle$ , and the one- and two-point correlation functions as a function of  $\Delta$  in increments of  $0.01$ . Then, we numerically

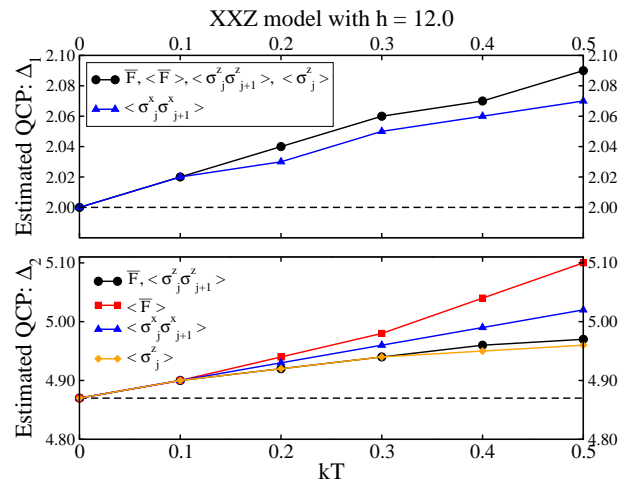


FIG. 6: (color online) Estimated QCPs after determining the extrema of the first order (upper panel) and of the second order (lower panel) derivatives with respect to  $\Delta$  for  $\overline{F}$ ,  $\langle \overline{F} \rangle$ ,  $\langle \sigma_j^x \sigma_{j+1}^x \rangle$ ,  $\langle \sigma_j^z \sigma_{j+1}^z \rangle$ , and  $\langle \sigma_j^z \rangle$  at several different values of  $T$ . See text for details on how the QCPs were estimated. The dashed lines mark the exact values of the QCPs.

computed the first order derivatives of those quantities about  $\Delta_1$  and their second order derivatives about  $\Delta_2$ . The values of  $\Delta$  leading to the greatest values for the magnitudes of those derivatives are shown in Fig. 6. If we take into account that  $\Delta$  was changed in increments of  $0.01$ , the spots of the maxima of the magnitudes of the first order derivatives are obtained within an accuracy of  $\pm 0.01$  about the values shown in the upper panel of Fig. 6. And since the second order derivatives are obtained from the first order ones, which already have a numerical error of  $0.01$ , we estimate that the error for the location of the maxima of the absolute values of the second order derivatives are at least  $\pm 0.02$  about the values shown in the lower panel. Excluding the data for  $T = 0$ , we made linear regressions with the remaining data ( $kT = 0.1, 0.2, 0.3, 0.4, 0.5$ ) in order to check whether a straight line would correctly predict the QCPs at  $T = 0$ . For all quantities shown in the upper panel of Fig. 6 and to all but one in the lower panel, the linear coefficients (y-axis intercepts) correctly predicted the QCPs within an accuracy of  $\pm 0.01$ . For  $\langle \overline{F} \rangle$ , however, we needed a quadratic regression to extrapolate to the correct value of  $\Delta_2$  with an accuracy of  $\pm 0.01$ .

To end this section we show in Figs. 7 and 8 the behavior of  $\langle \overline{F} \rangle$  as a function of  $\Delta$  for several temperatures and for the two external fields shown in Tab. I.

Looking at Figs. 7 and 8, we realize that now, contrary to the behavior of  $\overline{F}$  (see Figs. 2 and 3),  $\langle \overline{F} \rangle$  has only three instead of four derivative discontinuities at  $T = 0$ . Two of them are related to the two QCPs for this model while the remaining one is associated with the particular functional form of  $\langle \overline{F} \rangle$  [see Eq. (38)]. This third cusp of  $\langle \overline{F} \rangle$  is located at one of the values of  $\Delta$  in which  $|xx| = |zz|$  (left boundary of the yellow-shaded region in Fig. 9).

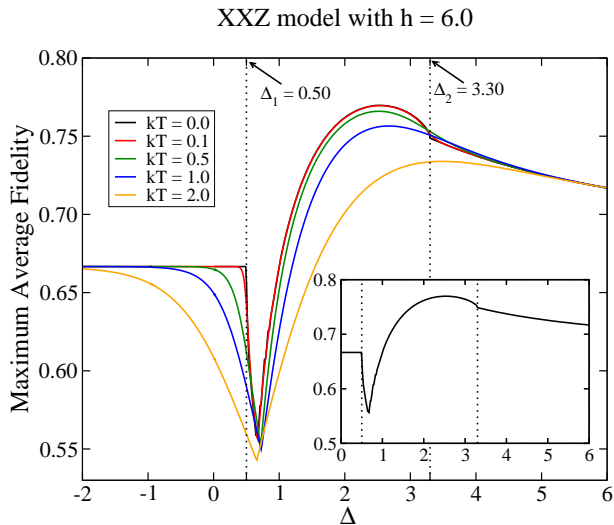


FIG. 7: (color online)  $\langle \overline{\mathcal{F}} \rangle$ , Eq. (38), as a function of  $\Delta$  with  $h = 6.0$  [see Eq. (16)]. At  $T = 0$  (see inset), both QCPs are detected by a discontinuity in the derivatives of  $\langle \overline{\mathcal{F}} \rangle$  with respect to  $\Delta$ . For  $T > 0$ , these discontinuities in the derivatives are smoothed out. The maximum (or minimum) of the derivatives are displaced away from the critical points. However, for  $kT \lesssim 0.5$  these extremum values lie close together and by extrapolating to  $kT \rightarrow 0$  we are able to infer the correct critical points. The dotted lines mark the QCPs and for the solid curves the temperature increases from top to bottom.

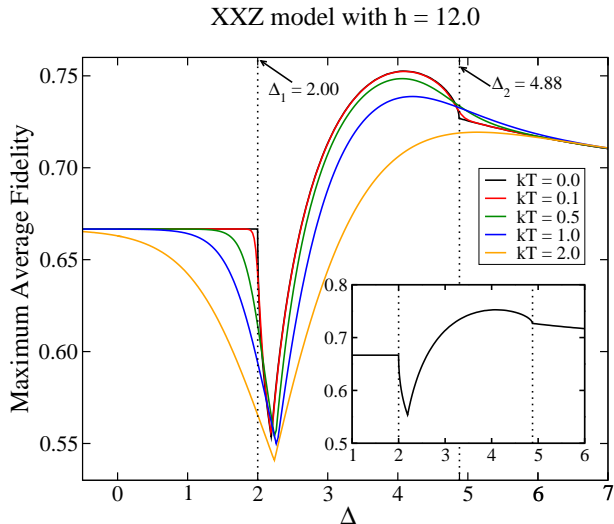


FIG. 8: (color online) Same as Fig. 7 but now  $h = 12.0$ . The dotted lines mark the QCPs and for the solid curves the temperature increases from top to bottom.

In order to understand the absence of the fourth cusp for  $\langle \overline{\mathcal{F}} \rangle$  at  $T = 0$ , we study the individual behavior of  $\langle \overline{F}(S_{\Psi\pm}) \rangle$  and  $\langle \overline{F}(S_{\Phi\pm}) \rangle$ , Eqs. (36) and (37), as a function of  $\Delta$ . Since  $\langle \overline{\mathcal{F}} \rangle$  is obtained by picking the greatest value among these four quantities, by tracing back which quantity gives  $\langle \overline{\mathcal{F}} \rangle$  we can understand the origin of the

cusplike behavior of  $\langle \overline{\mathcal{F}} \rangle$ .

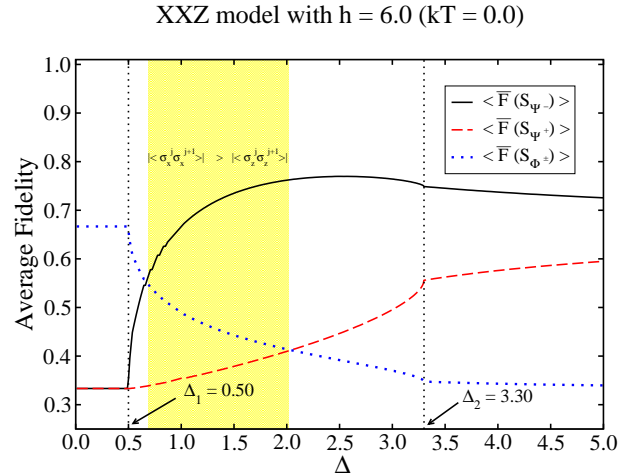


FIG. 9: (color online)  $\langle \overline{F}(S_k) \rangle$ , Eqs. (36) and (37), as a function of  $\Delta$  when  $T = 0$  and  $h = 6.0$ .

In Fig. 9 we show  $\langle \overline{F}(S_k) \rangle$  for  $k = \Psi^\pm, \Phi^\pm$  and fixing  $h = 6.0$  (a similar plot applies to  $h = 12.0$ ). Fig. 9 tells us that before the first QCP  $\Delta_1$  and up to where  $|xx| = |zz|$  for the first time, the maximum average fidelity  $\langle \overline{\mathcal{F}} \rangle$  is given by  $\langle \overline{F}(S_{\Phi\pm}) \rangle$ . Inside the yellow-shaded region, where  $|xx| > |zz|$ , and way up to and beyond the second QCP  $\Delta_2$ , the value of  $\langle \overline{\mathcal{F}} \rangle$  is dictated by  $\langle \overline{F}(S_{\Psi-}) \rangle$ . There is no change of the function that maximizes  $\langle \overline{\mathcal{F}} \rangle$  at the right boundary of the yellow-shaded region, contrary to what we see for  $\overline{\mathcal{F}}$  (Fig. 5). That is the reason we do not have a cusp equal where the two-point correlation functions become equal again ( $|xx| = |zz|$ ), at the right boundary of the yellow-shaded region. Furthermore, the two cusps related to the QCPs have their origin in the intrinsic functional form of  $\langle \overline{\mathcal{F}} \rangle$  that is not associated with  $\langle \overline{F}(S_{\Psi\pm}) \rangle$  and  $\langle \overline{F}(S_{\Phi\pm}) \rangle$  changing their roles in maximizing  $\langle \overline{\mathcal{F}} \rangle$ . Indeed, the cusps of  $\langle \overline{\mathcal{F}} \rangle$  at the two QCPs are a consequence of the cusps observed for the two-point correlation functions at those points. Since  $\langle \overline{\mathcal{F}} \rangle$  is a linear function of those correlation functions, any discontinuities in their derivatives with respect to  $\Delta$  will manifest themselves in discontinuities of the derivatives of  $\langle \overline{\mathcal{F}} \rangle$  (see Appendix A).

For  $T > 0$ , and similarly to the case of  $\overline{\mathcal{F}}$ , the cusps at the two QCPs that we see for  $\langle \overline{\mathcal{F}} \rangle$  at  $T = 0$  are smoothed out and displaced away. The other remaining cusp is not smoothed out although being displaced too. The procedure to estimate the QCPs using finite  $T$  data in the present case is exactly the same one reported for  $\overline{\mathcal{F}}$  a few paragraphs ago and the results of this analysis are given in Fig. 6.

#### IV. THE XY AND THE ISING MODEL

Using the notation of Sec. III, the anisotropic one-dimensional XY model subjected to a transverse mag-

netic field is described by the following Hamiltonian [42–44],

$$H = -\frac{\lambda}{4} \sum_{j=1}^L [(1 + \gamma) \sigma_j^x \sigma_{j+1}^x + (1 - \gamma) \sigma_j^y \sigma_{j+1}^y] - \frac{1}{2} \sum_{j=1}^L \sigma_j^z, \quad (42)$$

with  $\lambda$  being related to the inverse of the external magnetic field strength and  $\gamma$  the anisotropy parameter. If we set  $\gamma = \pm 1$  we have the transverse Ising model and for  $\gamma = 0$  we obtain the XX model in a transverse field.

As we change  $\lambda$  (essentially the external field), the ground state for the XY model goes through a QPT when we reach the QCP  $\lambda_c = 1.0$ . This is the Ising transition, where for  $\lambda < 1$  we have a ferromagnetic ordered phase and for  $\lambda > 1$  we have a quantum paramagnetic phase [45]. Whenever  $\lambda > 1$ , we also observe another QPT as we change the anisotropy parameter  $\gamma$ . It is called the anisotropy transition and it occurs at  $\gamma_c = 0$  [42–44, 46]. This QPT separates a ferromagnet ordered in the x-direction from a ferromagnet ordered in the y-direction. Although the  $\lambda$  and  $\gamma$  QPTs above are of the same order, they belong to different universality classes [42–44, 46].

The canonical ensemble density matrix describing the whole spin chain in equilibrium with a heat bath of temperature  $T$  is  $\varrho = e^{-H/kT}/Z$  and the density matrix describing a pair of nearest neighbors, obtained after tracing out all but those two spins, is [11, 47]

$$\rho_{23} = \begin{pmatrix} a & 0 & 0 & e \\ 0 & b & c & 0 \\ 0 & c & b & 0 \\ e & 0 & 0 & d \end{pmatrix}, \quad (43)$$

where

$$a = \frac{1 + 2 \langle \sigma_2^z \rangle + \langle \sigma_2^z \sigma_3^z \rangle}{4}, \quad (44)$$

$$b = \frac{1 - \langle \sigma_2^z \sigma_3^z \rangle}{4}, \quad (45)$$

$$c = \frac{\langle \sigma_2^x \sigma_3^x \rangle + \langle \sigma_2^y \sigma_3^y \rangle}{4}, \quad (46)$$

$$d = \frac{1 - 2 \langle \sigma_2^z \rangle + \langle \sigma_2^z \sigma_3^z \rangle}{4}, \quad (47)$$

$$e = \frac{\langle \sigma_2^x \sigma_3^x \rangle - \langle \sigma_2^y \sigma_3^y \rangle}{4}. \quad (48)$$

Similarly to the XXZ model of Sec. III, the translational symmetry of the XY model implies that  $\langle \sigma_j^\alpha \rangle = \langle \sigma_k^\alpha \rangle$  and  $\langle \sigma_j^\alpha \sigma_{j+1}^\beta \rangle = \langle \sigma_k^\alpha \sigma_{k+1}^\beta \rangle$ , for any value of  $j, k$ .

The computation in the thermodynamic limit and for arbitrary values of  $T$ ,  $\lambda$ , and  $\gamma$  of the one-point correlation function  $z = \langle \sigma_j^z \rangle = \text{Tr}[\sigma_j^z \varrho]$  and of the two-point correlation functions  $\alpha\alpha = \langle \sigma_j^\alpha \sigma_{j+1}^\alpha \rangle = \text{Tr}[\sigma_j^\alpha \sigma_{j+1}^\alpha \varrho]$ , where  $\alpha = x, y, z$ , is given in Refs. [42–44]. In Ref. [11] this solution is written in the present notation and in the Appendix B we show the behavior of  $\langle \sigma_j^z \rangle$  and  $\langle \sigma_j^\alpha \sigma_{j+1}^\alpha \rangle$

for  $T = 0$  and several values of  $\lambda$  and  $\gamma$ . We also give a brief qualitative discussion of how they differ from the  $T = 0$  case.

Proceeding along the same lines as in Sec. III, inserting Eqs. (1), (2), and (43) into Eq. (8) leads to the same set of probabilities  $Q_j(|\psi\rangle)$  for Alice measuring a given Bell state [cf. Eqs. (24) and (25)]. Using Eqs. (13), (24) and (25), the mean fidelity (14) for each one of Bob's four sets of unitary operations become

$$\overline{F}(|\psi\rangle, S_{\Psi^-}) = h(r, \chi, -xx, -yy, zz), \quad (49)$$

$$\overline{F}(|\psi\rangle, S_{\Psi^+}) = h(r, \chi, xx, yy, zz), \quad (50)$$

$$\overline{F}(|\psi\rangle, S_{\Phi^-}) = h(r, \chi, -xx, yy, -zz), \quad (51)$$

$$\overline{F}(|\psi\rangle, S_{\Phi^+}) = h(r, \chi, xx, -yy, -zz), \quad (52)$$

where

$$h(r, \chi, xx, yy, zz) = [1 + 2r^2(1 - r^2)(xx + yy + 2zz) - zz + 2r^2(1 - r^2)(xx - yy) \cos(2\chi)]/2. \quad (53)$$

Note that if we assume  $xx = yy$  in Eqs. (49)-(52), we obtain the corresponding expressions for the XXZ model, namely, Eqs. (27)-(30). That this should indeed occur can be seen by setting  $xx = yy$  in the two-qubit density matrix (43). In this case we recover the two-qubit density matrix for the XXZ model, Eq. (19), and consequently Eqs. (27)-(30) must follow from Eqs. (49)-(52) if we assume  $xx = yy$ .

Repeating the calculations of Ref. [20] that led to the optimum mean fidelity over all input states, it is not difficult to see that the extrema of Eq. (14) occur for the states  $|\psi\rangle = |0\rangle, |1\rangle$ , and  $(|0\rangle + e^{i\chi}|1\rangle)/\sqrt{2}$ . This gives

$$\overline{F}(S_{\Psi^\pm}) = \max \left[ \frac{1 \pm xx}{2}, \frac{1 \pm yy}{2}, \frac{1 - zz}{2} \right], \quad (54)$$

$$\overline{F}(S_{\Phi^\pm}) = \max \left[ \frac{1 \pm xx}{2}, \frac{1 \mp yy}{2}, \frac{1 + zz}{2} \right], \quad (55)$$

where  $\overline{F}(S_k)$  is given by Eq. (39). If we now maximize over the four possible sets of unitary operations available to Bob, we get the maximum of the mean fidelity (14) for the present model,

$$\begin{aligned} \overline{\mathcal{F}} &= \max_{\{|\psi\rangle, S_k\}} \overline{F}(|\psi\rangle, S_k) \\ &= \max \left[ \frac{1 + |xx|}{2}, \frac{1 + |yy|}{2}, \frac{1 + |zz|}{2} \right]. \end{aligned} \quad (56)$$

Averaging over all input states lying on the Bloch sphere [20], we get from Eqs. (15) and (49)-(52),

$$\langle \overline{F}(S_{\Psi^\pm}) \rangle = (3 \pm xx \pm yy - zz)/6, \quad (57)$$

$$\langle \overline{F}(S_{\Phi^\pm}) \rangle = (3 \pm xx \mp yy + zz)/6. \quad (58)$$

Using Eqs. (57) and (58), the maximum average fidelity is

$$\begin{aligned} \langle \overline{\mathcal{F}} \rangle &= \max_{\{S_k\}} \langle \overline{F}(S_k) \rangle \\ &= \max \left[ \frac{3 + |xx + yy| - zz}{6}, \frac{3 + |xx - yy| + zz}{6} \right]. \end{aligned} \quad (59)$$



Equations (56) and (59) are the analogs of Eqs. (35) and (38) for the present model. Note that if  $xx = yy$ , we recover Eqs. (35) and (38) from (56) and (59).

We now focus on studying the efficiency of Eqs. (56) and (59) in detecting the QCPs for the XY model in a transverse field at zero and non-zero temperatures. Following Ref. [11], we expect that the best way to pinpoint the QCP  $\lambda_c$  for the XY model is by studying the first and second order derivatives of Eqs. (56) and (59) with respect to  $\lambda$ . It turns out that the extremum values of the derivatives are located at this QCP for  $T = 0$  and move away as we increase  $T$ . For a sufficiently low range of temperatures, these extremum values lie on a straight line and by extrapolating to  $T = 0$  we can predict the correct QCP. Also, our numerical analysis showed that  $\overline{\mathcal{F}}$  is a better QCP detector than  $\overline{\mathcal{F}}$  when it comes to spotlighting the Ising transition ( $\lambda_c$ ), with the former having greater and sharper maximum (or minimum) about this QCP. Therefore, here we only show the behavior of  $\overline{\mathcal{F}}$  about this QCP.

In Figs. 10, 11, and 12 we show for several values of  $T$  and  $\gamma$  the behavior of  $\overline{\mathcal{F}}$  as a function of  $\lambda$ . For  $\gamma = 0.0$  we have the isotropic XX model in a transverse field. Looking at Fig. 10, we realize that at  $T = 0$  the QCP is determined by a discontinuity in the first derivative of  $\overline{\mathcal{F}}$ . For high values of  $T$  this discontinuity in the derivative is smoothed out and displaced from the exact location of the QCP, namely,  $\lambda_c = 1.0$ . However, as we will show in a moment, we still can determine the correct QCP using finite  $T$  data.

For the other values of  $\gamma$ , i.e.,  $\gamma = 0.5$  (anisotropic XY model in a transverse field) and  $\gamma = 1.0$  (Ising model in a transverse field), the QCP is determined by an inflection point that occurs exactly at  $\lambda_c = 1.0$  when  $T = 0$ . As we increase  $T$ , this inflection point moves away from  $\lambda_c$  and by determining the maximum (minimum) of the first and second order derivatives of  $\overline{\mathcal{F}}$  with respect to  $\lambda$  we can infer the correct QCP extrapolating from finite  $T$  data.

Two remarks are in order now. First, the behavior of  $\overline{\mathcal{F}}$  for all  $T$  and  $\gamma$  around  $\lambda_c$  is similar to the behavior of the two-point correlation functions about that point. This is true because  $\overline{\mathcal{F}}$  is essentially a linear function of the two-point correlation functions in the neighborhood of the QCP [cf. Eq. (56)]. Being more specific, the derivatives of  $\overline{\mathcal{F}}$  at and about the QCP are proportional to the derivatives of the two-point correlation function furnishing the greatest magnitude at and in the neighborhood of the QCP. Therefore, the functional behavior of  $\overline{\mathcal{F}}$  and its derivatives about the QCP is essentially the same as this correlation function about the QCP. Second, the cusp-like behavior seen in Figs. 10, 11, and 12 slightly away from the QCP is related to the point where  $|xx| = |zz|$  (see Figs. 20-22 in the Appendix B). Before the cusp,  $|zz| > |xx|$ , and after it,  $|zz| < |xx|$ . It is this fact and the particular functional form of  $\overline{\mathcal{F}}$  that lead to those cusps. This is similar to what we have found when dealing with the XXZ model in Sec. III.

Returning to the analysis of how to obtain the correct

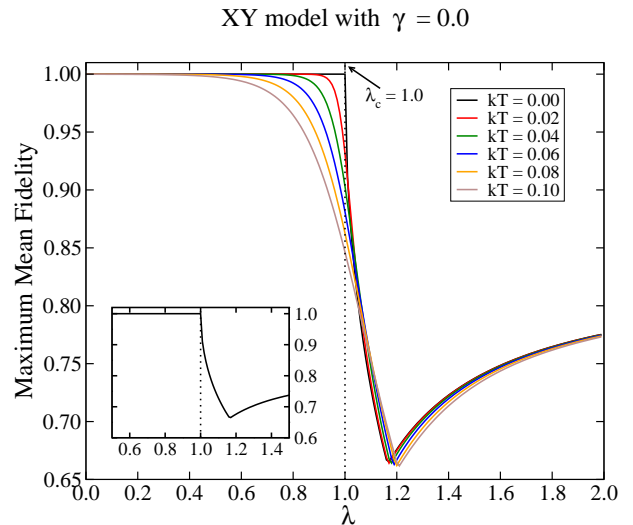


FIG. 10: (color online)  $\overline{\mathcal{F}}$ , Eq. (56), as a function of  $\lambda$  with  $\gamma = 0.0$  (XX model in a transverse field) [see Eq. (42)]. At  $T = 0$  (see the inset), the QCP  $\lambda_c = 1.0$  is detected by a discontinuity in the derivatives of  $\overline{\mathcal{F}}$  with respect to  $\lambda$ . For  $T > 0$ , these discontinuities in the derivatives are smoothed out. The maximum (or minimum) of the derivatives moves away from the QCP. However, for  $kT \lesssim 0.1$  these extremum values lie in a straight line and by extrapolating to  $kT \rightarrow 0$  we can discover the right value for the QCP. The dotted lines mark the QCP  $\lambda_c$  and for the solid curves the temperature increases from top to bottom when  $\lambda < \lambda_c$ .

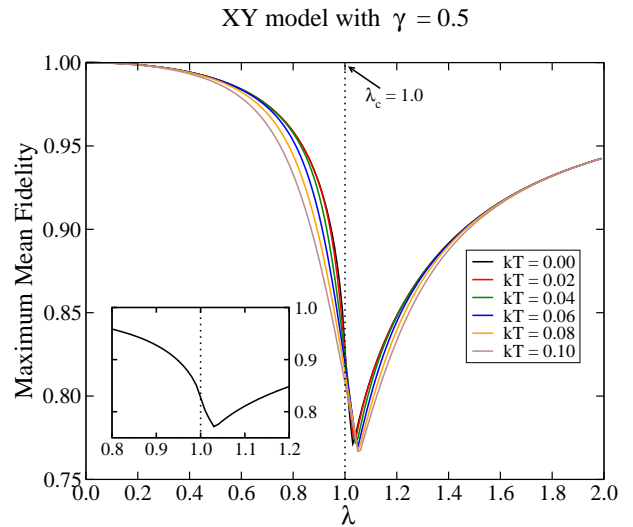


FIG. 11: (color online) Same as Fig. 10 but now  $\gamma = 0.5$ . The dotted lines mark the QCP  $\lambda_c$  and for the solid curves the temperature increases from top to bottom when  $\lambda < \lambda_c$ .

QCP using finite  $T$  data, we follow Ref. [11] and the procedure already explained in Sec. III, i.e., we numerically compute the first and second order derivatives of  $\overline{\mathcal{F}}$  around the QCP and search for their extremum values as indicators of a QPT. In Fig. 13 we plot as a function of  $T$  the value of  $\lambda$  (y-axis) furnishing the extrema of the

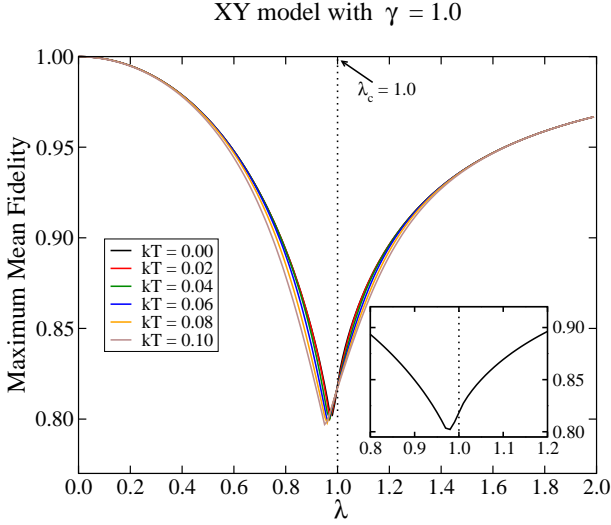


FIG. 12: (color online) Same as Fig. 10 but now  $\gamma = 1.0$  (Ising model in a transverse field). The dotted lines mark the QCP  $\lambda_c$  and for the solid curves the temperature increases from top to bottom before the kinks (minima).

first and second order derivatives of  $\overline{\mathcal{F}}$  with respect to  $\lambda$  in the neighborhood of the QCP  $\lambda_c$ .

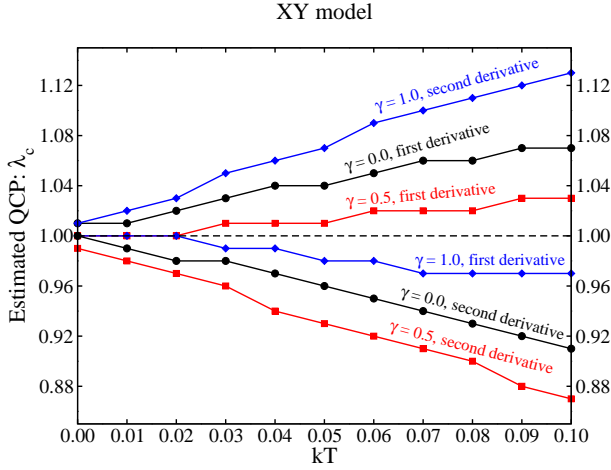


FIG. 13: (color online) Estimated value for the QCP  $\lambda_c$  using the location of the maximum (or minimum) of the first and second order derivatives of  $\overline{\mathcal{F}}$  with respect to  $\lambda$  for several values of  $T$ . See text for details. The dashed line gives the exact value of the QCP.

For the eleven values of  $kT$  shown in Fig. 13, namely,  $kT = 0.00, 0.01, 0.02, \dots, 0.10$ , we computed  $\overline{\mathcal{F}}$  as a function of  $\lambda$  in increments of 0.01. Subsequently, we numerically obtained its first and second order derivatives with respect to  $\lambda$ . The points shown in Fig. 13 are the location of the extrema of those derivatives. Similarly to what we had for the XXZ model, the locations of those extrema are obtained within an accuracy of  $\pm 0.01$  for the first derivatives and  $\pm 0.02$  for the second derivatives.

Dropping the data for  $kT = 0.00$ , we implemented a

simple linear regression with the remaining data ( $kT = 0.01, 0.02, \dots, 0.10$ ) to verify if a straight line could correctly predict the exact location of the QCP at  $kT = 0$ . For the six curves shown Fig. 13, the obtained linear coefficients (y-axis intercepts) predicted with an accuracy of 0.01 the correct location of  $\lambda_c$ .

Finally, in Figs. 14 and 15 we show, respectively,  $\overline{\mathcal{F}}$  and  $\langle \overline{\mathcal{F}} \rangle$  as functions of  $\gamma$ , fixing  $\lambda = 1.5$ . It is clear from the plots in both figures that the anisotropy QPT is clearly detected by both the maximum mean and maximum average fidelities.

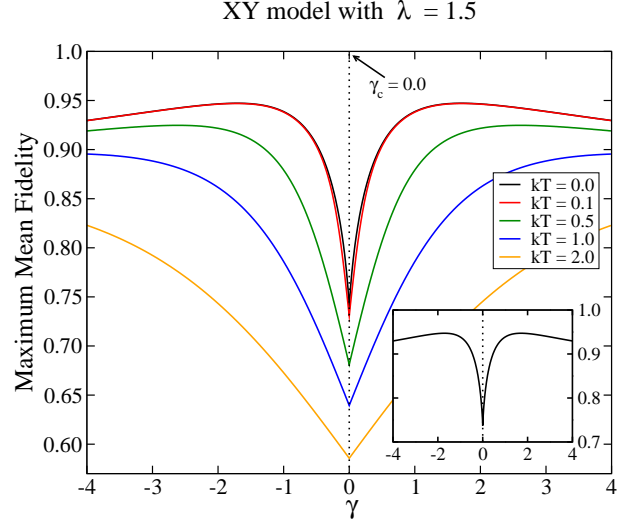


FIG. 14: (color online)  $\overline{\mathcal{F}}$ , Eq. (56), as a function of  $\gamma$  with  $\lambda = 1.5$  [see Eq. (42)]. Both at  $T = 0$  (see inset) and  $T > 0$ , the QCP  $\gamma_c = 0.0$  is detected by a cusp that occurs exactly at the location of the QPT. The dotted lines represent the QCP  $\gamma_c$  and for the solid curves the temperature increases from top to bottom.

The QCP  $\gamma_c = 0.0$  is detected by a cusp-like behavior of  $\overline{\mathcal{F}}$  for all values of  $T$  shown in Fig. 14. On the other hand, the cusp-like behavior of  $\langle \overline{\mathcal{F}} \rangle$  occurs only at  $T = 0$ , being smoothed out as we increase  $T$ . For higher values of  $T$ , the QCP is detected in this case by a local maximum of  $\langle \overline{\mathcal{F}} \rangle$  that occurs exactly at the correct location of the QCP. For high enough  $T$ , though, this maximum is flattened to the point of becoming useless in spotlighting the QCP.

The robustness of  $\overline{\mathcal{F}}$  to detect the anisotropy QPT can be traced back to its functional form and to the fact that it is exactly at  $\gamma_c = 0.0$  that  $xx = yy$ , with  $|xx| < |yy|$  right before  $\gamma_c$  and  $|xx| > |yy|$  right after it (see Fig. 23 in the Appendix B). This feature is not changed as we increase  $T$  and it is the reason why the cusps of  $\overline{\mathcal{F}}$  at  $\lambda_c$  are not smoothed out or displaced as we increase  $T$ . We should also remark that the two cusps that we see in Fig. 15 are not associated with QPTs. They are a consequence of the functional form of  $\langle \overline{\mathcal{F}} \rangle$  and to the following features (see Fig. 23 in Appendix B). At the first cusp of  $\langle \overline{\mathcal{F}} \rangle$ , which occurs for  $\gamma < \gamma_c$ ,  $|zz| = |xx|$ . Before this cusp we have  $|zz| > |xx|$  and after it  $|zz| <$

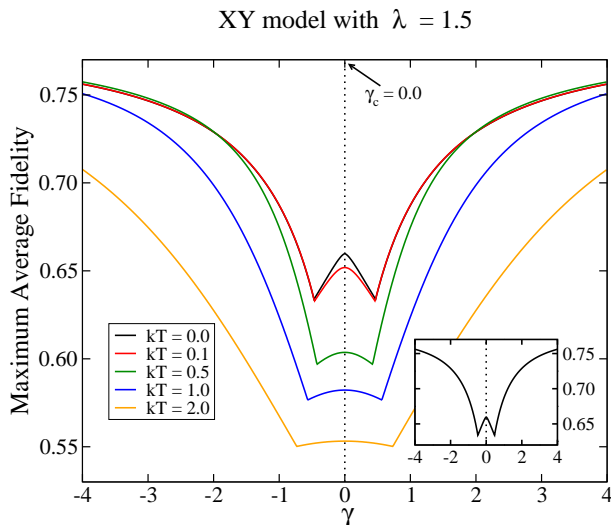


FIG. 15: (color online) Same as Fig. 14 but now we have  $\langle \overline{\mathcal{F}} \rangle$ , Eq. (59), as a function of  $\gamma$ . In this case the QCP is detected by a cusp at  $T = 0$ , with the latter being smoothed out as we increase  $kT$ . The dotted lines represent the QCP  $\gamma_c$  and for the solid curves the temperature increases from top to bottom.

$|xx\rangle$ . At the second cusp, which occurs for  $\gamma > \gamma_c$ ,  $|zz\rangle = |yy\rangle$ . Before this second cusp we have  $|zz\rangle < |yy\rangle$  and after it  $|zz\rangle > |yy\rangle$ . It is this exchange of the roles of which two-point correlation function gives the greatest magnitude that causes those two peaks. Note that those peaks do not show up in  $\overline{\mathcal{F}}$  because of its specific functional form, which implies that around those two locations it is only a function of either  $yy$  or  $xx$ . Contrary to  $\langle \overline{\mathcal{F}} \rangle$ , there is no role for  $zz$  in the functional form of  $\overline{\mathcal{F}}$  about the locations of the two peaks seen for  $\langle \overline{\mathcal{F}} \rangle$ . Thus, the above discussion that explains those peaks for  $\langle \overline{\mathcal{F}} \rangle$  does not apply to  $\overline{\mathcal{F}}$  and hence there is no reason for those peaks to appear in the functional behavior of  $\overline{\mathcal{F}}$ .

## V. DISCUSSION

The present proposal to detect quantum critical points (QCPs) with finite temperature data should be analyzed under two aspects. First, looking at its theoretical side, the most important piece of information we must have access to in order to calculate the fidelities  $\overline{\mathcal{F}}$  and  $\langle \overline{\mathcal{F}} \rangle$  is the density matrix describing a pair of qubits from the spin chain [Eqs. (19) or (43), for instance]. The two-qubit density matrix is obtained after tracing out all but two qubits from the canonical ensemble density matrix describing the whole chain in equilibrium with a thermal bath at temperature  $T$ . This two-qubit density matrix is a function of one- and two-point correlation functions and as such we must rely on analytical or numerical techniques to obtain those correlation functions to have access to the two-qubit density matrix.

The traditional way of characterizing quantum phase

transitions (QPTs), in particular at  $T = 0$ , is based on the knowledge of those correlation functions too. By studying their behavior as we change the system's Hamiltonian, or the behavior of quantities that are functions of them such as the magnetization or the magnetic susceptibility, we can detect QCPs by discontinuities in the  $n$ -th order derivative of those quantities that occur exactly at the QCPs. We can also employ quantum information theory based tools to detect QCPs, such as entanglement or quantum discord [5–8, 10, 11]. To apply these quantum information QCP detectors, we also need the correlation functions used in the traditional approach to characterize QPTs. The method we proposed in Ref. [20] and explored further here needs those correlation functions too.

However, some of these tools, such as the magnetization or magnetic susceptibility, may not properly identify the correct spot of the QCP with finite  $T$  data [11]. Other tools, such as the entanglement of formation [9], become zero at and around the QCP as we increase  $T$ , showing that they are useless in helping us in the identification of the QCP after a certain temperature threshold [11]. The tremendous success of quantum discord to spotlight QCPs at finite  $T$  came to the forefront in Ref. [11], where it was shown that for the XXZ model with no external field both QCPs are detected by discontinuities in the derivatives of quantum discord that occur at the exact location of the QCPs, even as we increase  $T$ . The present teleportation based tools to detect QCPs have the same remarkable attributes of quantum discord when detecting the QCPs for the XXZ model with no field [20]. However, a new theoretical feature sets them apart from any known finite temperature QCP detector that is as robust as the quantum discord: scalability as we increase the system's Hilbert space dimension.

Indeed, the evaluation of quantum discord is an NP-complete problem [14]. Thus, the calculation of quantum discord is an intractable problem for high spin systems [15]. On the other hand, the computational resources that are needed to calculate the maximum mean and maximum average fidelities are not so demanding. The maximum average fidelity  $\langle \overline{\mathcal{F}} \rangle$  is computed by repeating for each one of the four sets of unitary operations  $S_k$  the calculation of the average fidelity as given by Eq. (15). The computation of the latter is straightforward and can be scaled in an efficient way to an  $N$ -dimensional input state  $|\psi\rangle$  [20, 33]. The maximum mean fidelity  $\overline{\mathcal{F}}$  is computed by repeating four times the maximization of Eq. (14) over all input states  $|\psi\rangle$  (for each one of the four sets  $S_k$  of unitary operations available to Bob). This optimization problem is much less demanding than solving the optimization problem to determine the quantum discord or the entanglement of formation [20]. All things being equal, the tools created in Ref. [20] and further developed in this work to detect QCPs with finite  $T$  data should rank among the most efficient, scalable, and robust tools that are available in a theoretician tool box.

The second aspect under which the present proposal

should be analyzed is its experimental interpretation and feasibility. Contrary to quantum discord, the teleportation based tools to detect QCPs here developed have a clear operational interpretation. The experimental steps needed to teleport a qubit, namely, Bell state measurements and local unitary operations on single qubits, are clear and are not far from being implemented in spin-chain-like systems using state of the art techniques [48–54]. To experimentally determine Eqs. (14) and (15), all we need to know is Bob’s states at the end of several runs of the teleportation protocol using a representative sample of input states lying on the Bloch sphere as the states to be teleported from Alice to Bob. Moreover, in order to experimentally obtain Bob’s state once the teleportation protocol is implemented, we need to be able to measure the single spin density matrix describing Bob’s qubit. In other words, we only have to experimentally obtain one-point correlation functions. There is no need to measure two-point correlation functions anymore. Putting it differently, we can see the present proposal as a way to locally determine a QCP even when  $T > 0$ . There is no need to globally study the system in order to characterize its QPT with finite  $T$  data. Another approach where only local measurements are enough to study QPTs at  $T = 0$  can be built using the quantum energy teleportation protocol [27–30] and its possible extension in the theoretical framework of quantum networks [55–57].

It is also worth mentioning that from the experimental point of view, the time needed to implement all the steps of the teleportation protocol should be shorter than the time the system takes to return to equilibrium with the heat bath. The rate at which we execute the teleportation protocol must be greater than the relaxation rate of the system. We must also determine the state received by Bob at the end of the teleportation protocol before it equilibrates once again with the heat bath.

The theoretical computation of the relaxation time for an infinite spin chain is not trivial and lies beyond the scope of the present work. The relaxation time depends not only on the spin chain internal dynamics (its Hamiltonian) but also on how it interacts with the heat bath after a “disturbance” (the implementation of the teleportation protocol in our case). Experimentally, this relaxation time can be measured, for instance, by monitoring the magnetization of the system. In thermal equilibrium, the system’s magnetization has a definite value. When we perturb it, the magnetization changes. By monitoring the magnetization after the disturbance we can determine the time for the magnetization to get back to its equilibrium value. This time is the relaxation time, which is much easier to be measured than computed.

Furthermore, spin chains can be experimentally implemented on several different platforms. A few examples include quantum dots, quantum wells, and superconducting qubits. In GaAs quantum wells, for instance, we have at room temperature a relaxation time of a few nanoseconds [58]. In GaAs quantum dots the relaxation time of a spin-1/2 is measured to be around  $50 \mu s$  at  $T \approx 20mK$

[59] and in Ge/Si quantum dot arrays at  $T \approx 5K$  we get a relaxation time around  $10\mu s$  [60]. On the other hand, in silicon quantum dots at  $T \approx 1K$  one can execute single and two-qubit gates in a time span shorter than  $100ns$  [61]. This means that currently for silicon quantum dots and at low temperatures ( $\approx 1K$ ) we can, in principle, implement about one hundred gates before the system thermalizes. This is more than enough to implement the present proposal, which needs just a few gates at a given run of the teleportation protocol. We should also note that for superconducting qubits, we already have tens of qubits prepared simultaneously with coherence times of the order of  $100\mu s$ . The time needed to implement single and two-qubit gates in this setup range between  $10ns$  to  $100ns$ . This means that per coherence time we can implement between  $10^3$  to  $10^4$  gates [62].

## VI. CONCLUSION

We applied to several other models the teleportation based tools to detect quantum critical points (QCPs) that were first presented in Ref. [20]. We studied several spin-1/2 chains in the thermodynamic limit (infinite number of spins). First we studied the XXZ model in an external longitudinal magnetic field and then the Ising model, the isotropic XX model, and the anisotropic XY model, all of them in external transverse magnetic fields. For all these models we investigated the performance of those tools to correctly detect the QCP at zero and finite temperature.<sup>1</sup>

The key idea leading to the teleportation based tools to detect QCPs is the use of a pair of spins from the spin chain as the entangled resource to implement the teleportation protocol. An external spin from the chain (the input state) is then teleported to one spin of that pair. We showed that the efficiency of the teleportation protocol depends crucially on which quantum phase we prepare the spin chain. At the QCP, we observed an abrupt change in the efficiency of the teleportation protocol. The efficiency is quantified via the fidelity between the input state (Alice’s qubit) and the output state at the end of the protocol (Bob’s qubit).

For  $T = 0$  we verified that the maximum mean fidelity  $\overline{\mathcal{F}}$  and the maximum average fidelity  $\langle \overline{\mathcal{F}} \rangle$  have a cusp or an inflection point exactly at the QCPs. For  $T > 0$  many of these cusps are smoothed out and both these cusps and the inflection points move away from the cor-

---

<sup>1</sup> In the present work as well as in Ref. [20] we have dealt with local models only. However, the present quantum teleportation based tools to detect QCPs should work equally well for non-local ones. This is true since what matters most to the usefulness of the present tools is the fact that a QPT induces a drastic change in the system’s ground state. As such, the efficiency of the teleportation protocol should be affected as we cross the QCP irrespective of whether or not the interaction is local.

rect location of the QCPs. For finite  $T$  these cusps and inflection points can be determined by studying the magnitudes of the first and second order derivatives of  $\overline{\mathcal{F}}$  and  $\langle \overline{\mathcal{F}} \rangle$ . The magnitudes of these derivatives become very large around the location of the QCPs. Below a certain temperature threshold, the locations of the extrema for those derivatives lie in a straight line and by extrapolating to zero temperature we can predict the correct values of the QCPs.

The results of Ref. [20] and the ones shown here imply that the teleportation based tools to detect QCPs have the same important characteristics of quantum discord [11], one of the most reliable QCP detector for finite  $T$ . Both quantum discord and the teleportation based tools studied here can be applied without the knowledge of the order parameter related to the QPT and are very robust to temperature increases. In addition to that, the present tools have two important characteristics not shared with quantum discord [20]. First, they have a direct experimental meaning while quantum discord does not. Also, the computational resources that we need to theoretically calculate them is much less demanding than what is required to compute quantum discord. This fact allows us to scale the present tools to high spin systems.

Finally, looking at Figs. 2, 3, 10, 11, 12, and 14, we observe that for each model and for each phase transition the behavior of  $\overline{\mathcal{F}}$  is unique (a similar analysis applies to  $\langle \overline{\mathcal{F}} \rangle$ ). In other words, the fingerprint of a phase transition and its underlying model is unique. The functional behavior of  $\overline{\mathcal{F}}$  as we change the tuning parameter of the Hamiltonian and drive the system across the QCP is specific for each model. In this sense, by studying  $\overline{\mathcal{F}}$  we can not only detect a QCP but also pinpoint the underlying model that led to that phase transition.

### Acknowledgments

GR thanks the Brazilian agency CNPq (National Council for Scientific and Technological Development) for funding and CNPq/FAPERJ (State of Rio de Janeiro Research Foundation) for financial support through the National Institute of Science and Technology for Quantum Information. GAPR is grateful to the São Paulo Research Foundation (FAPESP) for financial support through the grant 2023/03947-0.

### Appendix A: Correlation functions for the XXZ model in an external field

The Hamiltonian describing the XXZ model in a longitudinal external magnetic field is given by Eq. (16). The solution to this model for arbitrary  $T$  is given by Refs. [36–39] and this solution was adapted to the present purposes in Ref. [11]. At the absolute zero temperature, the functional behavior of the non-null correlation functions is given by Figs. 16 and 17.

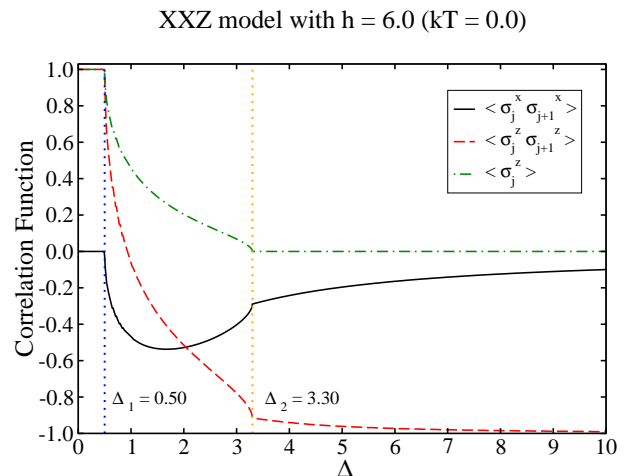


FIG. 16: (color online) One- and two-point correlation functions as a function of the tuning parameter  $\Delta$  with external magnetic field  $h = 6.0$ . All data were computed in the thermodynamic limit and at  $T = 0$ . The dotted lines mark the two QCPs for this model.

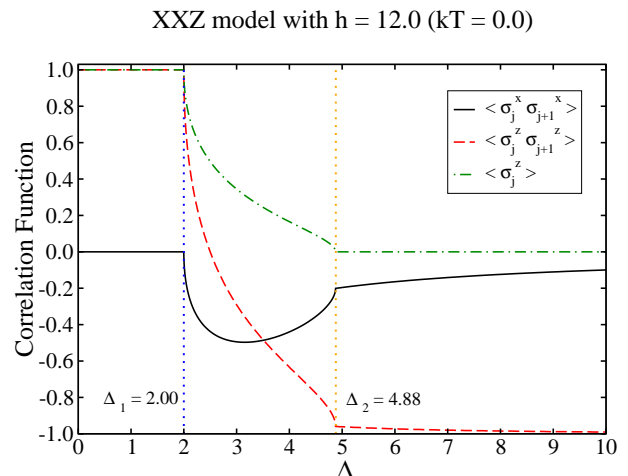


FIG. 17: (color online) Same as Fig. 16 but with  $h = 12.0$ .

For finite  $T$ , the correlation functions as a function of  $\Delta$  are given by Figs. 18 and 19.

### Appendix B: Correlation functions for the XY model subjected to an external field

The Hamiltonian describing the XY model subjected to a transverse external magnetic field is given by Eq. (42). This model was solved for arbitrary  $T$  in Refs. [42–44]. Using the present notation, a step-by-step description of this solution can be found in Ref. [11]. Note that two typos should be taken into account when consulting Ref. [11]. The Hamiltonian for the XY model there presented lacks an overall  $1/2$  factor and the expression for  $\langle \sigma_j^z \rangle$  should be multiplied by  $-1$ .

In Figs. 20, 21, and 22 we plot for  $T = 0$  the non-zero

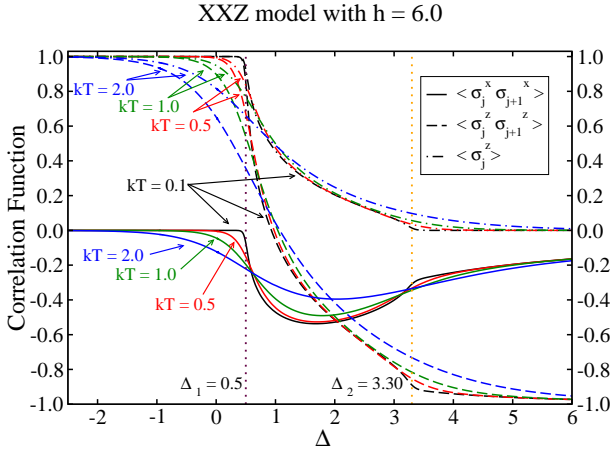


FIG. 18: (color online) One- and two-point correlation functions as a function of the tuning parameter  $\Delta$  with external magnetic field  $h = 6.0$ . All data were computed in the thermodynamic limit for several values of  $T > 0$ . The dotted lines mark the two QCPs for this model.

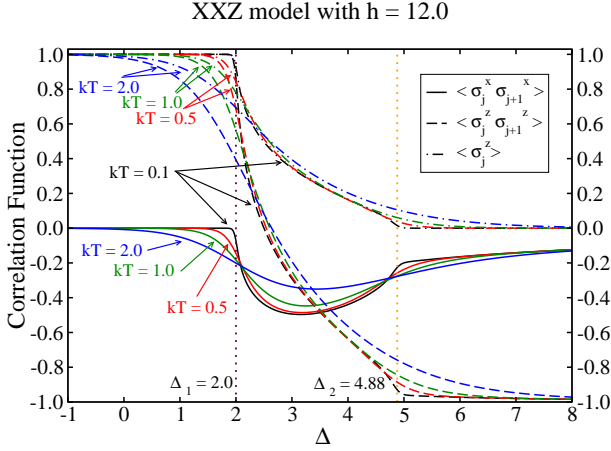


FIG. 19: (color online) Same as Fig. 18 but with  $h = 12.0$ .

correlation functions for this model as a function of  $\lambda$  for the three values of  $\gamma$  employed in the main text. Note that the case where  $\gamma = 1.0$  is the transverse Ising model.

For  $T = 0$  and fixing  $\lambda = 1.5$ , we show in Fig. 23 the relevant correlation functions as we change the anisotropy parameter  $\gamma$ .

The respective curves for  $T > 0$  have the general trends of the  $T = 0$  curves and we will not show them here. Similarly to what we see for the finite  $T$  curves of the XXZ model (see the Appendix A), as we increase the temperature the kinks are smoothed out and displaced from their locations at  $T = 0$ . Also, the magnitudes of the first and second order derivatives of the correlation functions at the QCPs decrease and are displaced from their  $T = 0$  locations.

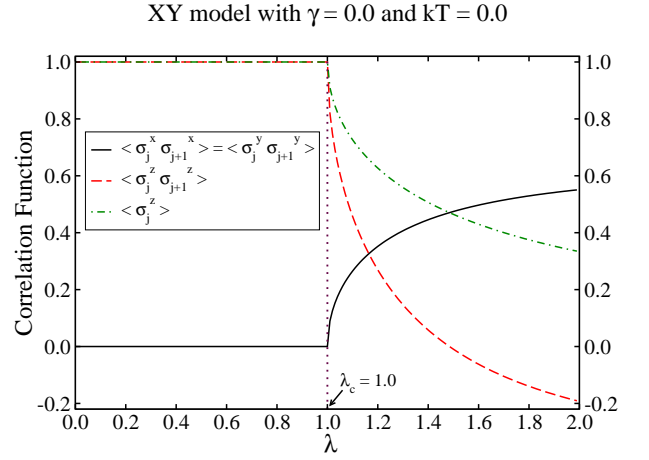


FIG. 20: (color online) One- and two-point correlation functions as a function of  $\lambda$ , the inverse strength of the field. Here  $\gamma = 0.0$ . All data were computed in the thermodynamic limit and at  $T = 0$ . The dotted vertical line marks the QCP for this model.

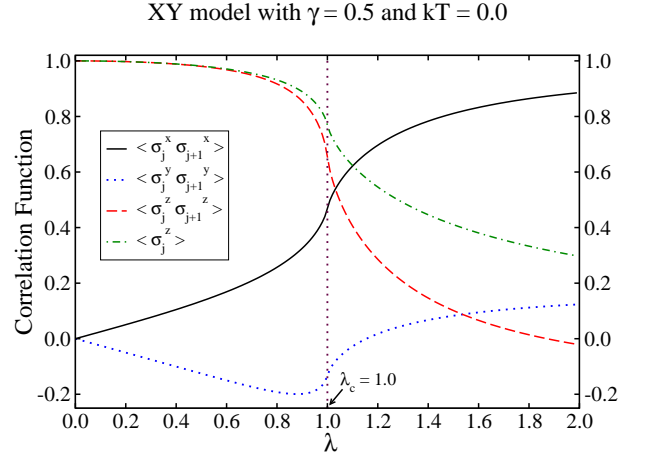


FIG. 21: (color online) Same as Fig. 20 but with  $\gamma = 0.5$ .

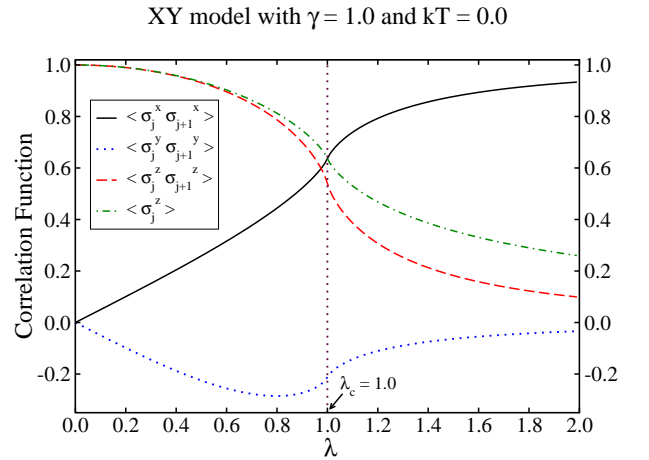


FIG. 22: (color online) Same as Fig. 20 but with  $\gamma = 1.0$ .

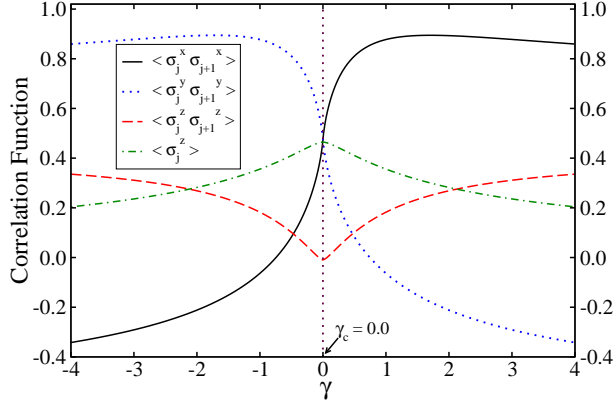
XY model with  $\lambda = 1.5$  and  $kT = 0.0$ 

FIG. 23: (color online) One- and two-point correlation functions as a function of  $\gamma$ , the anisotropy parameter. Here  $\lambda = 1.5$ . All data were computed in the thermodynamic limit and at  $T = 0$ . The dotted vertical line marks the QCP for this model.

- 
- [1] S. Sachdev, *Quantum Phase Transitions* (Cambridge University Press, Cambridge, 1999).
- [2] M. Greiner, O. Mandel, T. Esslinger, T. W. Hänsch, and I. Bloch, *Nature* (London) **415**, 39 (2002).
- [3] V. F. Gantmakher and V. T. Dolgoplov, *Phys. Usp.* **53**, 1 (2010).
- [4] S. Rowley, R. Smith, M. Dean, L. Spalek, M. Sutherland, M. Saxena, P. Alireza, C. Ko, C. Liu, E. Pugh *et al.*, *Phys. Status Solidi B* **247**, 469 (2010).
- [5] L.-A. Wu, M. S. Sarandy, and D. A. Lidar, *Phys. Rev. Lett.* **93**, 250404 (2004).
- [6] T. R. de Oliveira, G. Rigolin, M. C. de Oliveira, and E. Miranda, *Phys. Rev. Lett.* **97**, 170401 (2006); T. R. de Oliveira, G. Rigolin, and M. C. de Oliveira, *Phys. Rev. A* **73**, 010305 (2006); T. R. de Oliveira, G. Rigolin, M. C. de Oliveira, and E. Miranda, *Phys. Rev. A* **77**, 032325(R) (2008).
- [7] R. Dillenschneider, *Phys. Rev. B* **78**, 224413 (2008).
- [8] M. S. Sarandy, *Phys. Rev. A* **80**, 022108 (2009).
- [9] W. K. Wootters, *Phys. Rev. Lett.* **80**, 2245 (1998).
- [10] T. Werlang and G. Rigolin, *Phys. Rev. A* **81**, 044101 (2010).
- [11] T. Werlang, C. Trippé, G. A. P. Ribeiro, and G. Rigolin, *Phys. Rev. Lett.* **105**, 095702 (2010); T. Werlang, G. A. P. Ribeiro, and G. Rigolin, *Phys. Rev. A* **83**, 062334 (2011); T. Werlang, G. A. P. Ribeiro, and G. Rigolin, *Int. J. Mod. Phys. B* **27**, 1345032 (2013).
- [12] H. Ollivier and W. H. Zurek, *Phys. Rev. Lett.* **88**, 017901 (2001).
- [13] L. Henderson and V. Vedral, *J. Phys. A: Math. Gen.* **34**, 6899 (2001).
- [14] Y. Huang, *New J. Phys.* **16**, 033027 (2014).
- [15] A. L. Malvezzi, G. Karpat, B. Çakmak, F. F. Fanchini, T. Debarba, and R. O. Vianna, *Phys. Rev. B* **93**, 184428 (2016).
- [16] E. P. Wigner and M. M. Yanase, *Proc. Natl. Acad. Sci. USA* **49**, 910 (1963).
- [17] G. Karpat, B. Çakmak, and F. F. Fanchini, *Phys. Rev. B* **90**, 104431 (2014).
- [18] D. Girolami, *Phys. Rev. Lett.* **113**, 170401 (2014).
- [19] Y. C. Li, J. Zhang, and H. Q. Lin, *Phys. Rev. B* **101**, 115142 (2020).
- [20] G. A. P. Ribeiro and G. Rigolin, *Phys. Rev. A* **107**, 052420 (2023).
- [21] C. H. Bennett, G. Brassard, C. Crepeau, R. Jozsa, A. Peres, and W. K. Wootters, *Phys. Rev. Lett.* **70**, 1895 (1993).
- [22] Y. Yeo, e-print arXiv:quant-ph/0205014; Y. Yeo, *Phys. Rev. A* **66**, 062312 (2002).
- [23] R. Fortes and G. Rigolin, *Phys. Rev. A* **96**, 022315 (2017).
- [24] R. Fortes and G. Rigolin, *Phys. Rev. A* **92**, 012338 (2015); **93**, 062330 (2016).
- [25] M. Hotta, *Phys. Lett. A* **372**, 5671 (2008).
- [26] M. Hotta, *J. Phys. Soc. Jpn.* **78**, 034001 (2009).
- [27] K. Ikeda, *Phys. Rev. D* **107**, L071502 (2023).
- [28] K. Ikeda, *Phys. Rev. Appl.* **20**, 024051 (2023).
- [29] K. Ikeda, *AVS Quantum Sci.* **5**, 035002 (2023).
- [30] K. Ikeda, R. Singh, and R.-J. Slager, e-print arXiv:2310.15936 [quant-ph].
- [31] M. A. Nielsen and I. L. Chuang, *Quantum Computation and Quantum Information* (Cambridge University Press, Cambridge, 2000).
- [32] A. Uhlmann, *Rep. Math. Phys.* **9**, 273 (1976).
- [33] G. Gordon and G. Rigolin, *Phys. Rev. A* **73**, 042309 (2006); **73**, 062316 (2006); *Eur. Phys. J. D* **45**, 347 (2007).
- [34] C. N. Yang and C. P. Yang, *Phys. Rev.* **147**, 303 (1966).
- [35] J. Cloizeaux and M. Gaudin, *J. Math. Phys.* **7**, 1384 (1966).
- [36] A. Klümper, *Ann. Phys.* **1**, 540 (1992); *Z. Phys. B* **91**, 507 (1993).
- [37] M. Bortz and F. Göhmann, *Eur. Phys. J. B* **46**, 399 (2005).
- [38] H. E. Boos, J. Damerau, F. Göhmann, A. Klümper, J. Suzuki, and A. Weiße, *J. Stat. Mech.* (2008) P08010.
- [39] C. Trippé, F. Göhmann, and A. Klümper, *Eur. Phys. J. B* **73**, 253 (2010).
- [40] M. Takahashi, *Thermodynamics of one-dimensional solvable models* (Cambridge University Press, Cambridge, 1999).
- [41] G. A. P. Ribeiro and G. Rigolin, in preparation.
- [42] E. Lieb, T. Schultz, and D. Mattis, *Ann. Phys.* **16**, 407 (1961).
- [43] E. Barouch, B. M. McCoy, and M. Dresden, *Phys. Rev. A* **2**, 1075 (1970).
- [44] E. Barouch and B. M. McCoy, *Phys. Rev. A* **3**, 786 (1971).
- [45] P. Pfeuty, *Ann. Phys. (New York)* **57**, 79 (1970).
- [46] M. Zhong and P. Tong, *J. Phys. A: Math. Theor.* **43**, 505302 (2010).
- [47] T. J. Osborne and M. A. Nielsen, *Phys. Rev. A* **66**, 032110 (2002).
- [48] X. Rong, J. Geng, F. Shi, Y. Liu, K. Xu, W. Ma, F. Kong, Z. Jiang, Y. Wu, and J. Du, *Nat. Commun.* **6**, 8748 (2015).
- [49] C. E. Bradley, J. Randall, M. H. Abobeih, R. C. Berrevoets, M. J. Degen, M. A. Bakker, M. Markham, D. J. Twitchen, and T. H. Taminiau, *Phys. Rev. X* **9**, 031045 (2019).
- [50] T. Xie, Z. Zhao, X. Kong, W. Ma, M. Wang, X. Ye, P. Yu, Z. Yang, S. Xu, P. Wang *et al.*, *Sci. Adv.* **7**, eabg9204 (2021).
- [51] A. Noiri, K. Takeda, T. Nakajima, T. Kobayashi, A. Sammak, G. Scappucci, and S. Tarucha, *Nature* **601**, 338 (2022).
- [52] X. Xue, M. Russ, N. Samkharadze, B. Undseth, A. Sammak, G. Scappucci, and L. M. Vandersypen, *Nature* **601**, 343 (2022).
- [53] M. T. Mađzik, S. Asaad, A. Youssry, B. Joecker, K. M. Rudinger, E. Nielsen, K. C. Young, T. J. Proctor, A. D. Baczewski, A. Laucht *et al.*, *Nature* **601**, 348 (2022).
- [54] T. Xie, Z. Zhao, S. Xu, X. Kong, Z. Yang, M. Wang, Y. Wang, F. Shi, and J. Du, e-print arXiv:2212.02831 [quant-ph].
- [55] Y. Wang, Z.-Y. Hao, Z.-H. Liu, K. Sun, J.-S. Xu, C.-F. Li, G.-C. Guo, A. Castellini, B. Bellomo, G. Compagno, and R. L. Franco, *Phys. Rev. A* **106**, 032609 (2022).
- [56] S. P. Neumann, A. Buchner, L. Bulla, M. Bohmann, R. Ursin, *Nat. Commun.* **13**, 6134 (2022).
- [57] K. Ikeda, e-print arXiv:2301.11884 [quant-ph].
- [58] Y. Ohno, R. Terauchi, T. Adachi, F. Matsukura, and H.



- Ohno, Phys. Rev. Lett. **83**, 4196 (1999).
- [59] R. Hanson, B. Witkamp, L. M. K. Vandersypen, L. H. W. van Beveren, J. M. Elzerman, and L. P. Kouwenhoven, Phys. Rev. Lett. **91**, 196802 (2003).
- [60] A. F. Zinovieva, A. V. Dvurechenskii, N. P. Stepina, A. I. Nikiforov, and A. S. Lyubin, Phys. Rev. B **81**, 113303 (2010).
- [61] L. Petit, M. Russ, G. H. G. J. Eenink, W. I. L. Lawrie, J. S. Clarke, L. M. K. Vandersypen, and M. Veldhorst, Commun. Mater. **3**, 82 (2022).
- [62] J. M. Gambetta, J. M. Chow, and M. Steffen, npj Quantum Inf. **3**, 2 (2017).